Research Square

Preprints are preliminary reports that have not undergone peer review.
They should not be considered conclusive, used to inform clinical practice,
or referenced by the media as validated information.

Tracking coastal phosphorus delivery in deep time

Maxwell Lechte

maxlechte@gmail.com

University of Sydney https://orcid.org/0000-0002-3152-9009

Changle Wang

Institute of Geology and Geophysics

Leslie Robbins

University of Regina https://orcid.org/0000-0002-6931-5743

Galen Halverson

McGill University https://orcid.org/0000-0003-3061-7928

Malcolm Wallace

University of Melbourne

Kurt Konhauser

University of Alberta https://orcid.org/0000-0001-7722-7068

Latisha Brengman

University of Minnesota - Duluth https://orcid.org/0000-0002-8389-4550

Dongjie Tang

State Key Laboratory of Biogeology and Environmental Geology, Institute of Earth Sciences, China University of Geosciences (Beijing) https://orcid.org/0000-0002-0075-6671

Ashleigh van Smeerdijk Hood

University of Melbourne

Susannah Porter

University of California Santa Barbara https://orcid.org/0000-0002-4707-9428

Devon Cole

Hourglass Climate

Nir Galili

Weizmann Institute of Science

Itay Halevy

Weizmann Institute of Science https://orcid.org/0000-0002-7325-8139

Bo Wan

Institute of Geology and Geophysics，Chinese Academy of Sciences https://orcid.org/0000-0002-5896-9485

Article

Keywords:

Posted Date: October 26th, 2026

DOI: https://doi.org/10.21203/rs.3.rs-8857873/v1

License: This work is licensed under a Creative Commons Attribution 4.0 International License.
Read Full License

Additional Declarations: There is **NO** Competing Interest.

Tracking coastal phosphorus delivery in deep time

Maxwell Lechte[1,2,3]†*, Changle Wang[4]*†*, Leslie James Robbins[5], Galen Halverson[1], Malcolm Wallace[2], Kurt Konhauser[6], Latisha Brengman[7], Dongjie Tang[8, 9, 10], Ashleigh van Smeerdijk Hood[2], Susannah Porter[11], Devon Cole[12], Nir Galili[13], Itay Halevy[13], Bo Wan[4]

[1]Department of Earth and Planetary Sciences/GEOTOP, McGill University, Montréal, Canada
[2]School of Geography, Earth and Atmospheric Sciences, The University of Melbourne, Melbourne, Australia
[3]Current address: School of Geosciences, University of Sydney, Sydney, Australia
[4]State Key Laboratory of Lithospheric and Environmental Coevolution, Institute of Geology and Geophysics, Chinese Academy of Sciences, Beijing, China
[5]Department of Earth Sciences, University of Regina, Regina, Canada
[6]Department of Earth and Atmospheric Sciences, University of Alberta, Edmonton, Canada
[7]Department of Earth and Environmental Sciences, University of Minnesota Duluth, Duluth, U.S.A.
[8]State Key Laboratory of Geomicrobiology and Environmental Changes, China University of Geosciences, Beijing, China
[9]Frontiers Science Center for Deep-time Digital Earth, China University of Geosciences, Beijing, China
[10]Institute of Earth Sciences, China University of Geosciences, Beijing, China
[11]Department of Earth Science, University of California Santa Barbara, Santa Barbara, U.S.A.
[12]Hourglass Climate, Montclair, U.S.A.
[13]Department of Earth and Planetary Sciences, Weizmann Institute of Science, Rehovot, Israel

*Corresponding authors:
Maxwell Lechte, maxlechte@gmail.com
Changle Wang, wangcl@mail.iggcas.ac.cn

†These authors contributed equally to this work.

Phosphorus (P) availability exerts a first-order control on primary productivity, yet how the P cycle has changed in response to Earth's surface evolution is poorly constrained. While sedimentary archives can be used to track fluctuations in ancient seawater P availability, different rock types have yielded conflicting interpretations. Here we develop a multi-proxy sedimentary record by combining analysis of the P content of ironstones, which provide novel insights into coastal settings, with rock types from deeper environments: banded iron formations,

shales and phosphorites. Our record reveals that during the Archaean, inputs from continental weathering, hydrothermalism and regeneration of marine organic matter were limited. The early Palaeoproterozoic is widely hypothesised to have had elevated continental P fluxes, and this is reflected in coastal ironstone trends, likely due to continental emergence and intensified oxidative weathering. However, subsequent incomplete supercontinent breakup and low-relief orogens maintained lower P availability through the middle Proterozoic. Finally, elevated P contents in coastal and offshore archives, driven by marine oxygenation and crustal evolution in the Neoproterozoic, herald the emergence of a modern-like P cycle in which marine phosphate availability is governed by upwelling and organic matter oxidation. This new record reveals how tectonics, weathering, redox evolution and the biosphere interacted to progressively reshape the nutrient landscape that underlies biological productivity.

The availability of the macronutrient phosphate (PO_4^{3-}) has likely been the limiting factor for the productive capacity of the biosphere throughout most of Earth's history[1-3]. Phosphorus is primarily delivered to the modern ocean through the denudation of continental rocks[4] which, in addition to detrital P phases, can release bioavailable PO_4^{3-} from the chemical weathering of phosphate minerals. However, the vast majority of modern marine primary productivity is sustained by the remineralisation of organic P[3]. The oxygenation of the ocean–atmosphere system, together with major changes in changes in Earth's tectonics, climate, and the biosphere, has inevitably reshaped the

global P cycle over geological time, but the consequences for deep-time nutrient availability remain enigmatic[5].

Phosphate fluxes into the ocean are balanced on geological timescales by burial in marine sediments, making the geochemistry of ancient marine sedimentary rocks a valuable archive. Because PO_4^{3-} scavenging by Fe(III) (oxyhydr)oxides scales with ambient PO_4^{3-} concentrations[6], the abundance of authigenic phosphate in iron-rich marine chemical sedimentary rocks known as banded iron formations has been used as a proxy record for PO_4^{3-} availability in ancient seawater[7-11]. The lower P contents of Precambrian banded iron formations compared to their Phanerozoic counterparts have been interpreted to reflect limited marine PO_4^{3-} availability during this time due to effective sequestration by iron mineral precipitation in the water column[7,12]. This first-order trend is consistent with the lack of P-rich shales in the Precambrian[13]. However, bottom water anoxia can also enhance sedimentary P regeneration via organic matter degradation coupled to sulphate (SO_4^{2-}) reduction[14] and the dissolution of particulate P by hydrogen sulphide (H_2S) [15]. Consequently, the low P contents of Precambrian iron formations and shales has instead been interpreted to reflect greater regeneration from the sediment pile[16]. Given this ambiguity, models for deep-time marine PO_4^{3-} availability diverge significantly[5,8,17,18].

Crucially, previous compilations primarily use banded iron formations and shales[13] that reflect deposition in offshore basinal or shelf and slope settings, while coastal settings

have been largely overlooked. Yet, P availability and speciation vary significantly across modern marine environments[19], and this spatial heterogeneity could have been even greater in the redox-stratified oceans of Precambrian[2,3,5]. Indeed, major changes in Earth's surface evolution such ocean–atmosphere oxygenation in the Palaeoproterozoic and the Phanerozoic are considered to require high nutrient supply from the continents to the oceans[13,20,21], and these hypotheses need to be tested against the coastal sedimentary record. Unlike the largely deep-marine banded iron formations, oolitic ironstones are unique coastal iron deposits that are common in the Phanerozoic, and these contain phosphates derived from the upwelling and oxidation of organic matter[22,23]. Recently, Precambrian ironstones have also been shown to contain phosphates[24,25], highlighting their potential as a deep-time archive.

Ironstones are characterised by ooids composed of Fe (oxyhydr)oxides (hematite, goethite) and/or Fe silicates (berthierine, chamosite), hosted by coastal siliciclastic—carbonate successions[26], and commonly featuring microcrystalline phosphates (francolite, monazite, rhabdophane) within the ooid cortices. Because these phosphates are authigenic (and not detrital), their abundance depends on the availability of PO_4^{3-} in ancient coastal waters. Ironstones are distinct from iron formations, which are dominated by chert, Fe oxides (hematite, magnetite), Fe carbonates (siderite) and Fe silicates (stilpnomelane, greenalite). Most iron formations are laminated (i.e., banded) and were deposited below wave base, although some have a granular texture and record shallower depositional conditions. Here, we investigate the P geochemistry of coastal ironstones

through time, and integrate these data with an updated compilation of the iron formation and phosphorite records to provide a more complete assessment of marine P burial.

Compilation of sedimentary phosphorus records

Major element geochemical data were generated for 154 samples from 6 Proterozoic and 10 Phanerozoic ironstones (see Methods, Supplementary Information), alongside previously published data from 1345 samples across 130 ironstone deposits (Table S1). For iron formations, we compiled data from 4145 samples representing 217 deposits (Table S1), more than six times the data resolution of previous compilations[7,8]. Each iron formation deposit was assigned to a specific sub-category based on depositional setting: exhalative and continental margin banded iron formations from offshore settings, iron formations from glaciated margins, and granular iron formations from shallow marine environments (Fig. 1; see Methods). Here, we present P data as molar P/Fe ratios (conventionally P/Fe x 100; P/Fe*), although alternate normalisation approaches yield the same trends, supported by statistical analyses (Supplementary Figure 1; Table S1).

Our new ironstone record shows significant temporal complexity linked to major transitions in Earth's surface evolution. We can delineate five distinct stages in sedimentary P burial (I–V; Figs. 2–3): the Archaean (Stage I), the Palaeoproterozoic (Stage II), the Mesoproterozoic to early Neoproterozoic (Stage III), the subsequent Neoproterozoic (Stage IV), and the Phanerozoic (Stage V; see Extended Data Figure 1). The P/Fe* values of the ironstones and iron formations of these stages are summarised

in Table 1 and described in detail in the Supplementary Information. Below, we discuss the secular trends in P burial across these different depositional environments.

Limited early phosphorus availability in the Archaean

In the Archaean (Stage I), P burial is limited in both coastal and offshore environments (Table 1; Supplementary Information), which we interpret indicate a low PO_4^{3-} flux and limited organic P recycling. Under the essentially Archaean anoxic atmosphere, the P cycle would have operated fundamentally differently to the modern. It has been suggested that continental apatite weathering rates were accelerated by acid rain[27]; however, significant continental emergence did not occur until the mid–late Archaean[28] (Fig. 2e), and prior to this continental weathering rates were probably limited by the availability of fresh rock[27]. Our dataset does not constrain truly deep marine (i.e., abyssal) environments, where anoxic seafloor weathering and alteration could have supplied PO_4^{3-} to the deep oceans[29,30]. However, this process releases substantially less P per unit of CO_2 consumed than continental chemical weathering[31,32], and PO_4^{3-} release from oceanic crust would be inhibited by enhanced adsorption onto authigenic phyllosilicates (such as lizardite or greenalite) under Archaean conditions[33].

While the solubility of phosphate minerals could have been enhanced in the ferruginous oceans of the Archaean[17], we suggest that other output fluxes could have been dominant, such as P scavenging by authigenic iron minerals such as green rust[34], greenalite[33], and Fe(III) oxyhydroxides[7]—including those produced by Fe(II)-oxidising bacteria. In addition,

we suggest that the remaining bioavailable PO_4^{3-} could have been effectively exhausted by local autotrophs and buried as organic P, as hydrothermalism would have supplied H_2 and Fe^{2+} to sustain methanogens and anoxygenic photosynthesisers[2]. Following the advent of oxygenic photosynthesis, the availability of electron donors was no longer an issue for global primary productivity, and cyanobacteria would have consumed the continental weathering PO_4^{3-} inputs[2,35]. The remineralisation of organic matter would have been limited in the Archaean by a lack of terminal electron acceptors[36] and extracellular enzymes capable of degrading complex organic macromolecules[37], meaning that a much larger fraction of PO_4^{3-} taken up by primary productivity would be buried in marine sediments. Together, these processes likely limited nutrient availability for early cyanobacteria and maintained a small biosphere.

Intriguingly, some Archaean carbonate rocks have higher P/Ca ratios than more recent carbonates[18]. However, the low-P data in that study are dominated by Recent corals (prone to vital effects[38]) and Cenozoic carbonate sediments from abyssal, oligotrophic settings with important differences in mineralogy, diagenetic history and P dynamics compared to Neoarchaean shallow marine carbonates. Therefore, more carbonate data are needed to resolve this issue. Similarly, the observation of authigenic phosphates in iron formations has been cited as evidence that Archaean seawater PO_4^{3-} concentrations were sufficient for water-column nucleation and precipitation of apatite[29]. However, we instead suggest that these phosphates were more likely an early diagenetic product related to localised scavenging and organic matter degradation, consistent with previous interpretations[39]. Regardless, the P/Fe* values of Archaean exhalative iron formations

(with a median of 0.30, 95 % confidence interval of 0.28–0.32; n = 1006, 64 deposits) are approximately seven times lower than those from the Phanerozoic (median 2.14; 95 % confidence interval 1.85–2.24; n = 650, 35 deposits; see Table 1). This contrast is more consistent with low PO_4^{3-} availability in Archaean coastal habitats and upwelling deep waters.

Continental weathering drives Proterozoic phosphorus availability

The appearance of P-rich ironstones and coastal phosphorites during the Palaeoproterozoic (Stage II), despite low P burial in offshore settings (Figs. 2–3), suggests an increase in the continental PO_4^{3-} flux. The P/Fe* values of Stage II ironstones are significantly higher than middle Proterozoic ironstones (see Table 1), and because diagenesis, seawater P burial efficiency, or mineralogy would have been similar across these time periods, changes in coastal PO_4^{3-} fluxes were likely the primary control. Deposit-level comparisons suggest that at least parts of Stage II, in some basins, may be similar to the high-P Phanerozoic ironstone distributions (see Methods, Table S1). Importantly, the transition into Stage II broadly coincides with atmospheric oxygenation during the Great Oxidation Event (ca. 2.45–2.22 Ga), and the elevated P ironstones coincide with a major positive carbonate carbon isotope excursion (the Lomagundi–Jatuli Excursion) and organic carbon burial (ca. 2.32–2.0 Ga; Fig. 2f) hypothesised to have been driven by an increase in primary productivity and high PO_4^{3-} availability[21,31,40]. This is recorded by our ironstone archive, providing independent validation for this proxy. Several factors may have favoured continental over seafloor weathering leading into and during the Palaeoroterozoic, including greater continental emergence, intensified

tectonism and subaerial volcanism[28], and widespread denudation during major glaciations[41]. Together, these processes could have increased terrestrial weatherability and PO_4^{3-} fluxes[31].

In turn, surface oxygenation would have fundamentally altered the P cycle. Oxidation of Fe(II)-bearing minerals in continental rocks, such as biotite, enhanced fracturing and thick regolith development[42]. Concurrent oxidation of pyrite and siderite generated acidic weathering solutions[43], increasing the flux of continental Fe(III) and other cations, which may explain the first appearance of ironstones ca. 2.3 Ga[26]. Synsedimentary aluminium phosphate–sulphate minerals in Palaeoproterozoic ironstones record these acidic, oxidising weathering conditions[25], which would have increased the efficiency of apatite weathering relative to CO_2 consumption during weathering. This shift would have contributed to the development of kaolinite-bearing palaeosols—an efficient vector for transporting P to the oceans[40]—and the oxidation of continental organic matter would have temporarily increased the P flux to proximal environments.

The Great Oxidation Event would have also reshaped the marine P cycle. The contraction of the marine Fe reservoir, evidenced by the decline of continental margin iron formation deposition (ca. 2.3–2.2 Ga), would have diminished the importance of water column PO_4^{3-} scavenging by Fe minerals[7,33,34], shifting the locus of coupled Fe–P cycling from the water column into the sediment pile. Organic matter oxidation coupled to SO_4^{2-} reduction would have increased sedimentary PO_4^{3-} regeneration[44], though recycling in deep waters was

likely still limited by the low availability of terminal electron acceptors[3]. Due to their sporadic distribution, it is difficult to ascertain whether the fluctuations in the P contents of Palaeoproterozoic ironstones represent secular variation or spatial heterogeneity. In either case, we propose that dissolved P availability during the Palaeoproterozoic was largely restricted to shallow coastal environments supplied by continental weathering[3], rather than upwelling, consistent with the apparent decoupling between coastal and offshore sedimentary P records (Fig. 2; Table 1).

The Mesoproterozoic to early Neoproterozoic (Stage III) saw limited P burial in both nearshore and offshore environments (Figs. 2–3; Table 1), suggesting muted continental PO_4^{3-} fluxes and limited organic P remineralisation. The P contents of Stage III ironstones and iron formations are significantly lower than Stage II and later stages, a pattern that is not an artefact of sample size or pseudo-replication (see Methods and Table S1). On long timescales, continental P supply is ultimately regulated by uplift and denudation exposing fresh crustal rocks to weathering. Although orogenesis continued throughout the Proterozoic, the long-lived supercontinent Nuna only partially dispersed before the amalgamation of Rodinia[28,45] (Fig. 2e), and mechanically weak crust due to elevated Proterozoic geotherms (evidenced by high metamorphic thermal gradients[46]; Fig. 2e) would have manifested as low-relief orogens[45,47], further suppressing continental weathering. Comparatively low strontium isotope ($^{87}Sr/^{86}Sr$) ratios in middle Proterozoic carbonates[48] (Fig. 2e) are consistent with limited weathering of ancient, more radiogenic continental crust[49].

Ironstone and iron formation data from this time are limited by the relative scarcity of these deposits (rather than insufficient sampling), possibly owing to attenuated rifting, hydrothermalism, and continental-weathering derived cation fluxes. We posit that these observations align with a protracted period of tectonic stability and biogeochemical stasis during the middle Proterozoic.

A Neoproterozoic transition to an upwelling-dominated phosphorus cycle

The persistently low P burial that dominated much of the Precambrian ended in the mid–late Tonian Period with a rise in the P contents of ironstones and exhalative iron formations, together with the appearance of major phosphorites and P-rich shales (Figs. 2–3). Together, these records define the beginning of a transitional interval (Stage IV; mid-Tonian to Ediacaran) characterised by greater P burial and therefore increased P inputs to the marine realm. Elevated marine PO_4^{3-} availability is independently demonstrated through the first fossil evidence for phosphate biomineralisation ca. 0.81 Ga[50]. Our compilation shows that these changes began before the Snowball Earth glaciations (Fig. 2f), implying that these events were not solely responsible for a major reorganisation of the global P cycle. Instead, the protracted break-up of the supercontinent Rodinia likely intensified continental weathering, as supported by a progressive increase in carbonate $^{87}Sr/^{86}Sr$ ratios[51]. However, Neoproterozoic ironstones are rare[26], and Stage IV only saw a modest increase in P/Fe* ratios (Fig. 2). Importantly, the Tonian marks the onset of phosphorite genesis in deeper settings (discussed in Ref. [52]), which heralds a transition towards an upwelling-dominated P cycle characteristic of the modern oceans.

The Phanerozoic (Stage V) shows a further increase in P burial recorded by ironstones, exhalative iron formations, and phosphorites in tandem (Figs. 2–3). We interpret this pattern to indicate high PO_4^{3-} availability in seawater, supported by the acquisition of phosphatic skeletons independently in multiple animal clades during the early Phanerozoic[53]. Intriguingly, secular variations in P burial do not exhibit a clear correlation with the evolutionary history of silica biomineralisers (Fig. 2f), despite the potential for dissolved silica in seawater to passivate P sorption onto Fe oxyhydroxides[8,10]. While it remains debated whether the drawdown of the silica reservoir to modern levels occurred in the early Palaeozoic (due to siliceous sponges and radiolarians) or Cenozoic (driven by the expansion of diatoms[54]), the Tonian rise in exhalative iron formation P contents (Fig. 2) and the subsequent middle Phanerozoic decline is difficult to explain as being driven by changes in seawater silica concentrations alone (see Extended Data Figure 1). Further, experimental studies suggest that the inhibitory effect of dissolved silica on Fe–P scavenging is muted in seawater by the presence of seawater cations[11] such as Ca^{2+} and Mg^{2+}. Consequently, we infer that this secular increase in the P contents of Stage V iron formations and ironstones primarily tracks a first-order increase in marine PO_4^{3-} availability.

The transition into Stage V coincided with the widespread appearance ophiolites delineating suture zones in collisional and accretionary orogens[28], and metamorphic assemblages that reflect mantle cooling and cold continental subduction[46], implying a cooler, stronger lithosphere capable of generating higher-relief mountain belts. This

interval also experienced major orogenesis during the amalgamation of Gondwana[55], and providing exposure of fresh crustal rocks, and helping to increase the PO_4^{3-} flux to the oceans. This is consistent with greater weathering inputs from ancient crust implied by a rapid rise in strontium isotope ratios leading into Stage V (Fig. 2f), and generally high $^{87}Sr/^{86}Sr$ values persist throughout the Phanerozoic[48]. The average P contents of the weatherable crust are inferred to have increased significantly between ca. 600–400 Ma[20], likely due to this episode of enhanced continental denudation stripping the continents of ancient, P-poor rock, and this would have augmented the trend towards greater marine PO_4^{3-} availability.

Against this backdrop, other processes would have varied continental PO_4^{3-} fluxes throughout the Phanerozoic. The evolution of land plants in the Ordovician and subsequent expansion of rooted vascular plants during the Devonian (Fig. 2g; Extended Data Fig. 1) would have enhanced soil development, mineral weathering, and PO_4^{3-} leaching, while also promoting clay mineral production[40,56], and coastal P burial was high during this interval. A middle Phanerozoic decline in $^{87}Sr/^{86}Sr$—interpreted to reflect reduced silicate weathering of continental interiors of Pangaea due to aridification[57]—coincides with an apparent decline in P content of ironstones and exhalative iron formations, which are rare during this time (Fig. 2c; Extended Data Fig. 1). Subsequent supercontinent breakup would have dispersed the continents, flooded their extensive margins, and increased mantle outgassing; conditions that would have favoured the deposition and preservation of ironstones and exhalative iron formations[58], and may have contributed to the renewed rise in P burial beginning in the Mesozoic. While the temporal

resolution of available data is insufficient to confidently resolve these higher-order relationships, the broad Phanerozoic increase in P burial across both coastal and basinal environments is consistent across proxies and statistically robust (Table S1).

In addition to these weathering controls, we propose that the apparent coupling between the coastal and offshore records reflects the emergence of a modern-like world where marine P availability is controlled by upwelling-driven nutrient recycling. The regeneration of organic P was likely limited by oxidant availability[3,36] until progressive oxygenation during the Neoproterozoic–Palaeozoic[59] ultimately ventilated the deep oceans. This marine oxygenation, itself fuelled by increased nutrient inputs, would have increased the relative importance of inorganic P burial sinks due to the enhanced recycling of organic matter which would, in turn, have sustained primary productivity[3,36]. In sum, our new findings provide new constraints on P availability at the land–sea interface—a critical juncture for nutrient supply to marine ecosystems—and lend support to independent hypotheses for increased PO_4^{3-} availability in the early Palaeoproterozoic and the Phanerozoic. This demonstrates how Earth's tectonic, climatic and redox evolution has shaped the long-term P cycle, and by extension, the size and complexity of the biosphere.

Figures

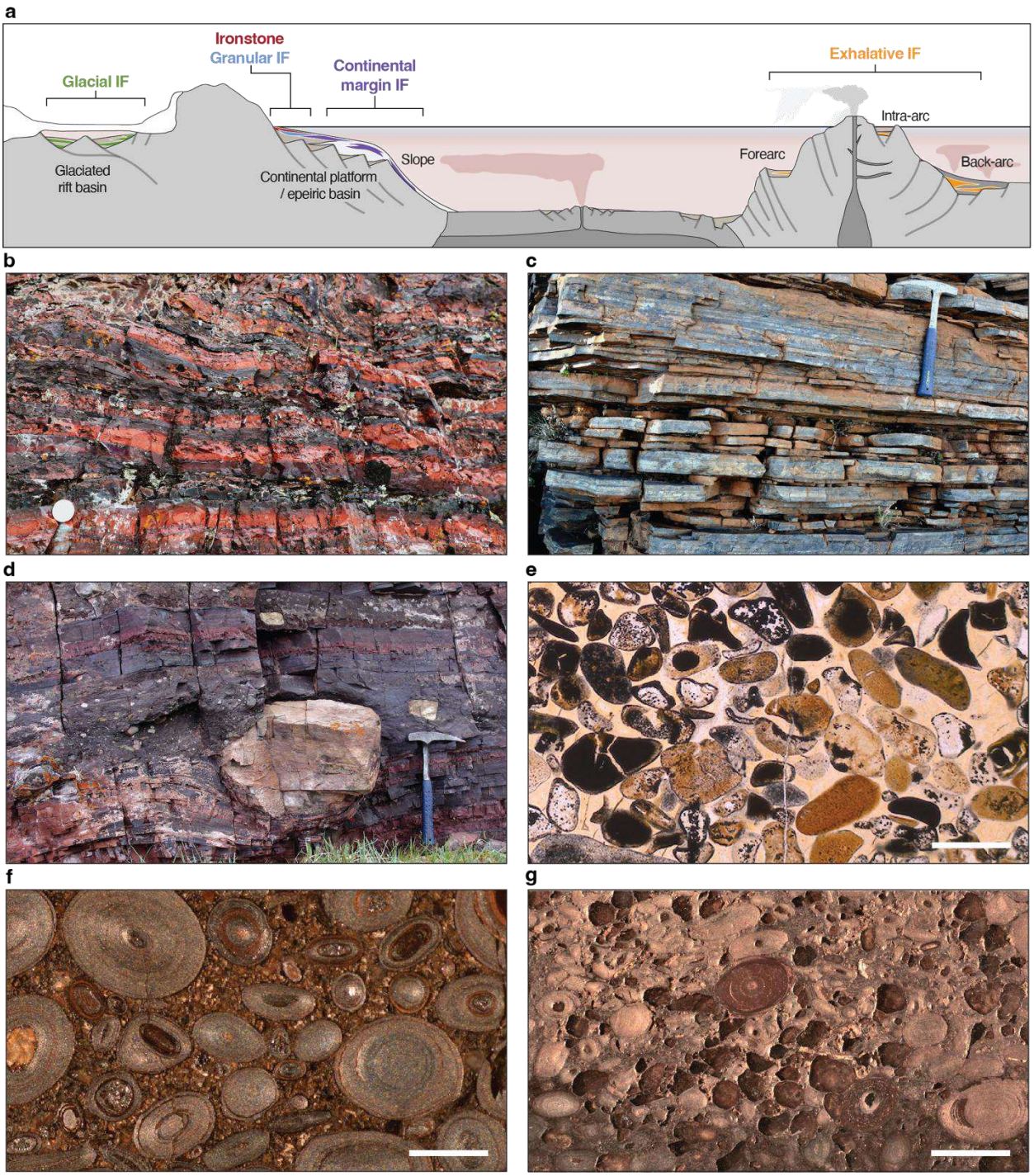


Fig. 1. Geological context of the studied lithologies. **a.** Tectonic setting and depositional environment of ironstones and the various iron formation (IF) types used to reconstruct P

burial. **b.** Lenticular, exhalative IF (bedded jasper, hematite) associated with hydrothermal breccias. Calymmian Wernecke Breccia, Yukon, Canada. **c.** Widespread, continental margin IF (bedded chert, Fe oxides and siderite) overlying carbonate platform deposits. Siderian Kuruman IF, South Africa. **d.** Dropstone in glacial IF (laminated hematite, chert) associated with diamictites. Cryogenian Rapitan Formation, Northwest Territories, Canada. **e.** Transmitted light photomicrograph of granular IF (granules of Fe phyllosilicates and Fe oxides in chert matrix). Orosirian Frere Formation, Western Australia. **f.** Incident light photomicrograph of oolitic ironstone (Fe oxide ooids in siliciclastic matrix). Statherian Chuanlinggou Formation, North China. **g.** Incident light photomicrograph of oolitic ironstone (Fe oxide ooids in siliciclastic matrix). Cambrian Bliss Formation, New Mexico, USA. Scale in panels e, f and g is 1 mm.

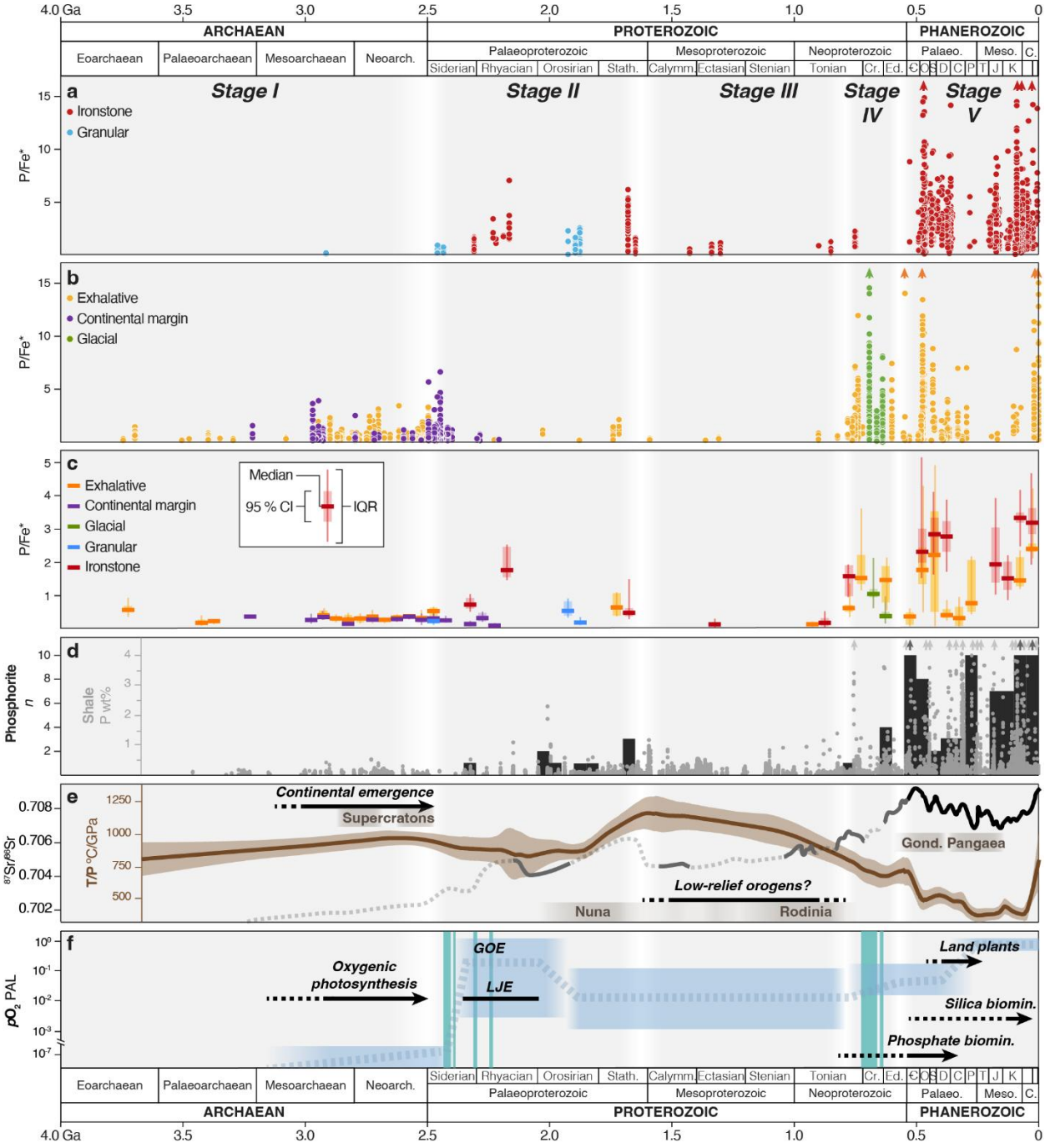


Fig. 2. The evolution of the P cycle in five intervals (Stages I–V), as delineated by various sedimentary archives. **a.** Compilation of P/Fe* values for shallow marine ironstones and granular iron formations. Arrows represent extreme P enrichments (P/Fe* > 15). **b.** P/Fe* values for exhalative, continental margin and glacial iron formations. Arrows represent

extreme P enrichments (P/Fe* > 15). **c.** Median values (horizontal bars) with 95 % confidence intervals (CI; boxes) and interquartile range (vertical lines) for the P/Fe* data in panels a and b (note the change in scale), binned into 50-million-year time intervals. Intervals with insufficient samples (n < 15) are not shown. **d.** Histogram of occurrences of major (i.e., metre-scale) phosphorite deposits (black; updated from Ref. [52]), binned into the same 50-million-year intervals. Arrows indicate intervals with more than 10 major phosphorite deposits. Shown in grey are the bulk-rock P contents of marine shales (data from Ref. [52] updated with new shale data from the Sedimentary Geochemistry Project, Ref. [60]); arrows represent extreme P enrichments (i.e., above 4 wt. %). **e.** Compiled seawater Sr isotope curve for Phanerozoic (black line[48]) and Precambrian (dark grey represents the curve based upon high-confidence data, dashed line represents the medium-confidence data of Ref. [49]). Also shown are details regarding the secular evolution of the Earth's crust[28], as well as a locally weighted scatterplot smoothing (LOWESS) fit through the thermobaric ratios of the metamorphic record[46] (dark brown line; lighter brown envelope represents 2σ bootstrap uncertainty). **f.** The fossil record of phosphate biomineralising organisms (dashed line apatitic scales[50]; solid line phosphatic animal shells[53]), silica biomineralising organisms[54] (dashed line sponges and radiolarians, solid line diatoms), and land plants (dashed line possible cryptospores, trilete spores, solid line vascular plants[61]). Also shown as blue rectangles is the range of estimates for atmospheric O_2 (relative to present atmospheric levels; PAL) adapted from Ref. [52], highlighting the Great Oxidation Event (GOE) and Lomagundi–Jatuli Excursion (LJE) [21] Vertical bars indicate periods of global glaciation in the Palaeoproterozoic and Neoproterozoic.

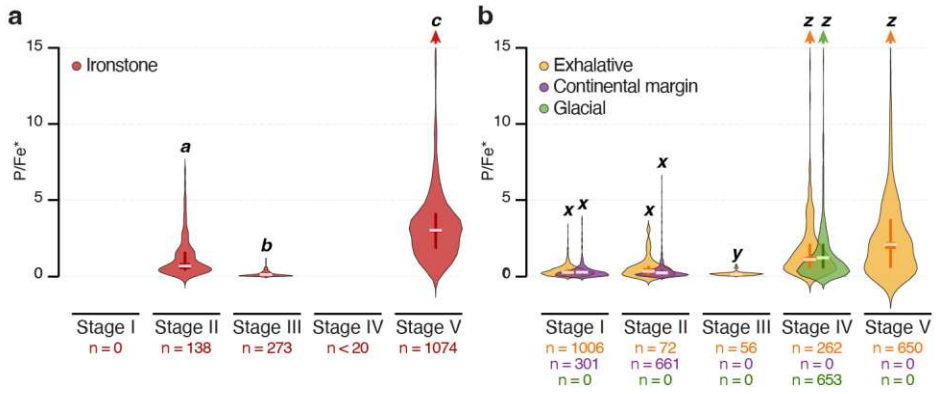


Fig. 3. P/Fe* distributions for **a.** ironstones and granular iron formations, and **b.** exhalative, continental margin and glacial iron formations, grouped into five time intervals (Stage I–V; see Fig. 2). Violin plots show kernel density estimates of distributions whereby the width is proportional to the data density. Pale dashes indicate the median (with the dark box indicating the 95 % confidence interval estimate); dark lines indicate the interquartile range. Note that P/Fe* values are truncated at 15 for visualization; the tails of distributions for ironstones and iron formations in Stages IV and V extend beyond this limit. Numbers below each violin denote sample size (n); bins with small sample sizes (n < 20) are not shown and were excluded from statistical comparison. Letters above violins based on pairwise distribution comparisons: groups sharing the same letter show no strong evidence for distributional differences (Kolmogorov-Smirnov tests with Benjamini-Hochberg false discovery rate correction; strong evidence defined as $p < 0.001$ and Cliff's delta > 0.474). Note that comparisons are only made between distributions of sample data from the same lithology across different time bins, and ironstone data are not quantitatively compared to iron formation data.

References

1 Tyrrell, T. The relative influences of nitrogen and phosphorus on oceanic primary production. *Nature* **400**, 525 (1999).

2 Stüeken, E. E. Exploring productivity hotspots in the Precambrian biosphere. *Philosophical Transactions of the Royal Society B: Biological Sciences* **380**, 20240103 (2025).

3 Laakso, T. A. & Schrag, D. P. A small marine biosphere in the Proterozoic. *Geobiology* **17**, 161-171 (2019).

4 Filippelli, G. M. in *Soil phosphorus* 1-22 (CRC Press, 2016).

5 Guilbaud, R. Proterozoic evolution of the phosphorus cycle: Was it high or was it low? *Treatise on Geochemistry* **5**, 153-175 (2025).

6 Feely, R. A., Trefry, J. H., Lebon, G. T. & German, C. R. The relationship between P/Fe and V/Fe ratios in hydrothermal precipitates and dissolved phosphate in seawater. *Geophysical Research Letters* **25**, 2253-2256 (1998).

7 Bjerrum, C. J. & Canfield, D. E. Ocean productivity before about 1.9 Gyr ago limited by phosphorus adsorption onto iron oxides. *Nature* **417**, 159 (2002).

8 Planavsky, N. J. *et al.* The evolution of the marine phosphate reservoir. *Nature* **467**, 1088 (2010).

9 Geijer, P. Some aspects of phosphorus in Precambrian sedimentation. *Ark. Miner. Geol.* **3**, 165-186 (1962).

10 Konhauser, K. O., Lalonde, S. V., Amskold, L. & Holland, H. D. Was there really an Archean phosphate crisis? *Science* **315**, 1234-1234 (2007).

11 Jones, C., Nomosatryo, S., Crowe, S. A., Bjerrum, C. J. & Canfield, D. E. Iron oxides, divalent cations, silica, and the early earth phosphorus crisis. *Geology* **43**, 135-138 (2015).

12 Rego, E. S. *et al.* Low-phosphorus concentrations and important ferric hydroxide scavenging in Archean seawater. *PNAS nexus* **2**, pgad025 (2023).

13 Reinhard, C. T. *et al.* Evolution of the global phosphorus cycle. *Nature* **541**, 386 (2017).

14 Ingall, E. D., Bustin, R. & Van Cappellen, P. Influence of water column anoxia on the burial and preservation of carbon and phosphorus in marine shales. *Geochimica et Cosmochimica Acta* **57**, 303-316 (1993).

15 Dijkstra, N., Hagens, M., Egger, M. & Slomp, C. P. Post-depositional formation of vivianite-type minerals alters sediment phosphorus records. *Biogeosciences* **15**, 861-883 (2018).

16 Poulton, S. W. Early phosphorus redigested. *Nature Geoscience* **10**, 75-76 (2017).

17 Brady, M. P., Tostevin, R. & Tosca, N. J. Marine phosphate availability and the chemical origins of life on Earth. *Nature Communications* **13**, 5162 (2022).

18 Ingalls, M., Grotzinger, J. P., Present, T., Rasmussen, B. & Fischer, W. W. Carbonate-associated phosphate (CAP) indicates elevated phosphate availability in Neoarchean shallow marine environments. *Geophysical Research Letters* **49**, e2022GL098100 (2022).

19 Duhamel, S. *et al.* Phosphorus as an integral component of global marine biogeochemistry. *Nature Geoscience* **14**, 359-368 (2021).

20 Walton, C. R. *et al.* Evolution of the crustal phosphorus reservoir. *Science Advances* **9**, eade6923 (2023).

21 Hodgskiss, M. S., Crockford, P. W. & Turchyn, A. V. Deconstructing the Lomagundi-Jatuli carbon isotope excursion. *Annual Review of Earth and Planetary Sciences* **51**, 301-330 (2023).

22 Matheson, E. J., Malone, J. D., Pufahl, P. K. & Hiatt, E. E. Late Ordovician ironstone and its relation to ocean redox instability, climate and glaciation. *Sedimentology* **72**, 631-665 (2025).

23 Pufahl, P. K. *et al.* Ordovician ironstone of the Iberian margin: Coastal upwelling, ocean anoxia and Palaeozoic biodiversity. *The Depositional Record* **6**, 581-604 (2020).
24 Johnson, B. R. *et al.* Phosphorus burial in ferruginous SiO2-rich Mesoproterozoic sediments. *Geology* **48**, 92-96 (2020).
25 Xie, B. *et al.* Marine aluminum phosphate–sulfate authigenesis as a phosphorus sink during mid-Proterozoic oxygenation. *Geophysical Research Letters* **51**, e2023GL107512 (2024).
26 Lechte, M. *et al.* Oolitic ironstones, continental iron flux and reverse weathering in the Proterozoic Eon: insights from the Tonian Katherine Group, Yukon. (2024).
27 Hao, J., Knoll, A. H., Huang, F., Hazen, R. M. & Daniel, I. Cycling phosphorus on the Archean Earth: Part I. Continental weathering and riverine transport of phosphorus. *Geochimica et Cosmochimica Acta* **273**, 70-84 (2020).
28 Cawood, P. A. *et al.* Secular evolution of continents and the Earth system. (2022).
29 Rasmussen, B., Muhling, J. R., Suvorova, A. & Fischer, W. W. Apatite nanoparticles in 3.46–2.46 Ga iron formations: Evidence for phosphorus-rich hydrothermal plumes on early Earth. *Geology* (2021).
30 Syverson, D. D. *et al.* Nutrient supply to planetary biospheres from anoxic weathering of mafic oceanic crust. *Geophysical Research Letters* **48**, e2021GL094442 (2021).
31 Mills, B., Lenton, T. M. & Watson, A. J. Proterozoic oxygen rise linked to shifting balance between seafloor and terrestrial weathering. *Proceedings of the National Academy of Sciences* **111**, 9073-9078 (2014).
32 Ouyang, S. *et al.* Phanerozoic onset of massive continental weathering. *Geophysical Research Letters* **52**, e2025GL117072 (2025).
33 Cui, X. *et al.* Phyllosilicate adsorption limited phosphorus bioavailability in early ferruginous oceans. *Nature Communications* (2026).
34 Sugiyama, I. & Halevy, I. Interaction of metal oxyions and phosphate with carbonate green rust: Insights into Earth's modern and ancient environments. *Geochimica et Cosmochimica Acta* **397**, 96-112 (2025).
35 Watanabe, Y., Ozaki, K. & Tajika, E. Marine phosphate level during the Archean constrained by the global redox budget. *Geophysical Research Letters* **51**, e2023GL108077 (2024).
36 Kipp, M. A. & Stüeken, E. E. Biomass recycling and Earth's early phosphorus cycle. *Science advances* **3**, eaao4795 (2017).
37 Mahmoudi, N., Steen, A. D., Halverson, G. P. & Konhauser, K. O. Biogeochemistry of Earth before exoenzymes. *Nature Geoscience* **16**, 845-850 (2023).
38 Crockford, P. & Halevy, I. Questioning the paradigm of a phosphate-limited Archean biosphere. *Geophysical research letters* **49**, e2022GL099818 (2022).
39 Li, Y.-L., Konhauser, K. O., Cole, D. R. & Phelps, T. J. Mineral ecophysiological data provide growing evidence for microbial activity in banded-iron formations. *Geology* **39**, 707-710 (2011).
40 Hao, W. *et al.* The kaolinite shuttle links the Great Oxidation and Lomagundi events. *Nature communications* **12**, 2944 (2021).
41 Papineau, D. Global biogeochemical changes at both ends of the Proterozoic: insights from phosphorites. *Astrobiology* **10**, 165-181 (2010).
42 Brantley, S., Lebedeva, M. & Bazilevskaya, E. in *The Atmosphere-History* 327-352 (Elsevier Inc., 2013).
43 Konhauser, K. O. *et al.* Aerobic bacterial pyrite oxidation and acid rock drainage during the Great Oxidation Event. *Nature* **478**, 369 (2011).
44 Alcott, L. J., Mills, B. J., Bekker, A. & Poulton, S. W. Earth's Great Oxidation Event facilitated by the rise of sedimentary phosphorus recycling. *Nature Geoscience* **15**, 210-215 (2022).

45 Spencer, C. J., Mitchell, R. N. & Brown, M. Enigmatic Mid-Proterozoic orogens: Hot, thin, and low. *Geophysical research letters* **48**, e2021GL093312 (2021).
46 Brown, M., Aulbach, S. & Johnson, T. Eclogites and eclogites: Implications for Archean tectonics. *Geology* (2026).
47 Ibrahim, Y. & Rey, P. F. From wide rifts to orogens: A new perspective for Proterozoic tectonics. *Geology* (2026).
48 McArthur, J., Howarth, R., Shields, G. & Zhou, Y. in *Geologic time scale 2020* 211-238 (Elsevier, 2020).
49 Chen, X., Zhou, Y. & Shields, G. A. Progress towards an improved Precambrian seawater 87Sr/86Sr curve. *Earth-Science Reviews* **224**, 103869 (2022).
50 Cohen, P. A., Strauss, J. V., Rooney, A. D., Sharma, M. & Tosca, N. Controlled hydroxyapatite biomineralization in an~ 810 million-year-old unicellular eukaryote. *Science Advances* **3**, e1700095 (2017).
51 Halverson, G. P., Dudás, F. Ö., Maloof, A. C. & Bowring, S. A. Evolution of the 87Sr/86Sr composition of Neoproterozoic seawater. *Palaeogeography, Palaeoclimatology, Palaeoecology* **256**, 103-129 (2007).
52 Planavsky, N. J. *et al.* A sedimentary record of the evolution of the global marine phosphorus cycle. *Geobiology* **21**, 168-174 (2023).
53 Kouchinsky, A. *et al.* Chronology of early Cambrian biomineralization. *Geological Magazine* **149**, 221-251 (2012).
54 Conley, D. J. *et al.* Biosilicification drives a decline of dissolved Si in the oceans through geologic time. *Frontiers in Marine Science* **4**, 397 (2017).
55 Collins, A. S. & Pisarevsky, S. A. Amalgamating eastern Gondwana: the evolution of the Circum-Indian Orogens. *Earth-Science Reviews* **71**, 229-270 (2005).
56 Lenton, T. M., Daines, S. J. & Mills, B. J. COPSE reloaded: An improved model of biogeochemical cycling over Phanerozoic time. *Earth-Science Reviews* **178**, 1-28 (2018).
57 Wang, R. *et al.* The coupling of Phanerozoic continental weathering and marine phosphorus cycle. *Scientific reports* **10**, 5794 (2020).
58 Van Houten, F. & Arthur, M. A. Temporal patterns among Phanerozoic oolitic ironstones and oceanic anoxia. *Geological Society, London, Special Publications* **46**, 33-49 (1989).
59 Wallace, M. W. *et al.* Oxygenation history of the Neoproterozoic to early Phanerozoic and the rise of land plants. *Earth and Planetary Science Letters* **466**, 12-19 (2017).
60 Farrell, Ú. C. *et al.* The Sedimentary Geochemistry and Paleoenvironments Project Phase 2 data release: An open data resource for the study of Earth's environmental history. *Chemical Geology*, 123311 (2026).
61 Servais, T. *et al.* Revisiting the Great Ordovician Diversification of land plants: Recent data and perspectives. *Palaeogeography, Palaeoclimatology, Palaeoecology* **534**, 109280 (2019).

Methods

Bulk-rock geochemical analyses

For bulk-rock geochemical analyses, well-preserved and representative samples were cut with a diamond-edge rock saw to remove weathered surfaces and crushed in an agate

mill to a fine powder. Approximately 50 mg of sample powder was dissolved in Teflon beakers using concentrated HF and HNO_3 at 95 ºC for 24 hours, dried down, and subsequently dissolved again using aqua regia at a ratio of 1:3 HNO_3 to HCl at 95 ºC for 48 hours. If undigested sample powder remained after the aqua regia addition, samples were centrifuged to remove any insoluble residue, and the supernatant was transferred into Teflon beakers and evaporated. Final residues were dissolved in 5 ml of 6 N HCl to generate stock solutions for geochemical measurements. A small aliquot (~10 µL) of the stock solution was then dried down and brought up in 4 ml of 5% HNO_3 containing an internal spike of 1 ppb Indium. The resulting solutions were analysed in the Department of Earth and Planetary Sciences at Yale University by inductively coupled plasma mass spectrometry using a ThermoFisher Scientific Element XR to determine selected major and trace element concentrations using a standard sample introduction system. Measurement precision was generally better than 5 % (2σ) for major and trace elements. USGS geostandards BHVO-2 and NOD-A-1 processed along with samples during each analytical run were within 5% of reported values for Fe and P.

Compilation of ironstones and iron formations through time

We analysed 106 samples from five different Proterozoic ironstone deposits, including: the ca. 2310 Ma Timeball Hill Formation from South Africa; the ca. 1650 Ma Chuanlinggou Formation from North China; the ca. 1320 Ma Sherwin Formation from northern Australia; the ca. 850 Ma McClure Formation from Yukon, Canada; and the ca. 750 Ma Galeros Formation Arizona, USA (the youngest-known Proterozoic ironstone[26]). Our results were compared to Phanerozoic ironstones, for which data were collected from 48 new samples

spanning 10 different deposits. The geological setting of the studied units were described in detail in Ref. [62]. These ironstone data are supplemented with literature data comprising 1345 samples from 130 distinct ironstone deposits spanning ca. 2310–5 Ma (Supplementary Information; Table S1). All analysed ironstones, regardless of age, were deposited in nearshore environments (i.e., coastal, lagoonal, shoreface and shallow subtidal settings) and share a broadly consistent mineralogy, featuring variable compositions of Fe(III) (oxyhydr)oxides (goethite / hematite) and Fe phyllosilicates (berthierine / chamosite), and are hosted by mixed siliciclastic—carbonate successions[26,63].

To contextualise the insights from ironstones relative to the iron formations record, we conducted an extensive literature survey of the major element composition of iron formations and marine hydrothermal iron deposits across Earth's history. We define four different types of iron formations based upon their mineralogy, texture and host stratigraphy (and therefore depositional environment): granular, continental margin, exhalative and glacial iron formations. Compiled iron formation geochemical data was assigned to one of these four categories based upon the described stratigraphic associations from the source literature. Granular iron formations (490 samples from 14 deposits from the literature, 27 new analyses) are composed of sand-sized grains of iron minerals (Fig. 1e) and occasionally feature iron ooids and cross lamination, indicative of deposition in a shallow marine environment (above wave base). Their distinct mineralogy, consisting predominantly of chert, Fe (oxyhydr)oxides (hematite, magnetite), Fe carbonates (siderite) and Fe silicates (stilpnomelane, minnesotaite, greenalite),

distinguishes these deposits from ironstones. Continental margin iron formations (962 samples from 55 deposits) are characterised by fine laminae (i.e., banded texture; Fig. 1c) of iron minerals with a similar mineralogy to granular iron formations. These units are stratigraphically bounded by siliciclastic and carbonate rocks and were deposited predominantly below storm-wave base in platform and upper slope settings. Exhalative iron formations (2040 samples from 128 deposits from the literature, 6 new analyses) formed in tectonically active settings near volcanic rocks (Fig. 1b), driven by hydrothermal activity, and were deposited below wave base. These are broadly equivalent to the 'Algoma type' iron formations[64] common in Archaean greenstone belts. The mineralogy of exhalative iron formations is similar to that of continental margin iron formations. Glacial iron formations (653 samples from 20 deposits) are unique to the Cryogenian Period (ca. 0.72–0.635 Ga) and formed in rift and intracontinental basins associated with glacial sedimentation (diamictites, dropstones) during the 'Snowball Earth' ice ages[65] (Fig. 1d). These deposits are dominated by hematite and are variably cherty[65]. Due to the fundamental mineralogical differences between ironstones and iron formations, we do not believe that P/Fe* values can be quantitatively compared between the two, and therefore we only evaluate trends within each lithology. However, the iron formation classification framework outlined above provides a robust basis for comparing P burial and Fe cycling across iron formation types and time periods and qualitatively comparing the resultant secular variation to that of the ironstone record.

Normalisation of data and statistical analyses

To evaluate the temporal evolution of P in different environments, we normalise P contents to Fe (where P/Fe* represents the molar ratio of P to Fe multiplied by 100) to mitigate dilution effects from siliciclastic input or chert, consistent with previous studies[7,8]. The P/Fe* values display strong non-normal distributions, necessitating non-parametric approaches. Alternative metrics and normalisation approaches (for example, bulk phosphorus concentrations, phosphorus–aluminium ratios, or mean values) do not change our first-order interpretation, as P content exerts the strongest influence on the observed trends (Fig. S1).

To characterise the secular variation of P/Fe* values for each lithology through time, we first assigned samples into 50 Ma time bins. While extreme P enrichments (e.g., bulk P contents >1 wt.%) may reflect important processes, they are uncommon and may partly result from detrital P enrichment. Central tendencies were therefore characterised using medians and third quartiles (3Q), with uncertainty in the median estimated using trimmed bootstrap resampling with replacement (5% trimming, 5,000 replicates) for data within time bins that included at least 15 samples. The 95 % confidence intervals were defined by the 2.5th and 97.5th percentiles of the bootstrap distribution (Fig. 2c).

Following this, we tested the hypothesis that these data showed statistically significant differences across the different stages outlined in the text by grouping samples by lithology and age into one of these five groups (Stages I–V). Distribution-level differences among groups of samples from the same lithology (Fig. 3) were evaluated using pairwise

two-sample Kolmogorov–Smirnov tests, with p-values corrected for multiple comparisons using a false-discovery-rate procedure. Only time bins containing at least 20 samples of the same lithology were retained for statistical comparisons. The magnitude and direction of differences were quantified using Cliff's delta, a rank-based effect size, and evidence for differences was classified using a tiered framework: strong evidence ($p < 0.001$ and $|\delta| > 0.474$), moderate evidence ($p < 0.01$ and $|\delta| > 0.33$), and suggestive evidence ($p < 0.05$ and $|\delta| > 0.147$). Only differences meeting strong or moderate evidence thresholds were used to define statistically distinct groups, providing a conservative basis for interpretation (Fig. 3). Statistical comparisons of bulk-rock P contents produce similar results to comparisons using P/Fe* ratios. To assess whether these differences are inflated by pseudo-replication (i.e., large numbers of analyses from the same deposits dominating a group's distribution), we also ran these comparisons treating each deposit, rather than each individual sample, as the unit of replication. For each deposit, we calculated the median P/Fe* value, and performed comparisons between the deposits of the same lithology for each stage (as described above) using stage-level medians and pairwise Kolmogorov–Smirnov tests with Cliff's delta effect sizes. The results of these comparisons are shown in Table S1.

To evaluate whether the lower P/Fe* values of the Precambrian stages could reflect the product of insufficient sampling relative to the Phanerozoic, we performed a rarefaction analysis for stage comparisons involving an imbalance in sample sizes, i.e., Stage III versus Stage V. Specifically, we compared Stage III (the middle Proterozoic) to Stage V (the Phanerozoic), as Stage III has relatively few ironstones (n = 273) and exhalative iron

formations (n = 60) versus stage V (n = 1082 and 650 respectively). For each comparison, we repeatedly drew, without replacement, random subsamples (10,000 replicates) from the well-sampled Phanerozoic (Stage V) population, with each subsample matched in size to the corresponding Precambrian stage. In both cases fewer than 1 in 10,000 subsamples of Stage V produced medians or 90th percentiles as low as those observed in Stage III, and maximum values were similarly low ($p < 0.0001$). This analysis suggests that sample size alone cannot explain the observed differences.

Interpreting ancient seawater P concentrations from ironstone and iron formation geochemistry

To translate bulk-rock P contents into estimates of synsedimentary P authigenesis, it is necessary to consider sedimentary and post-depositional processes that could have affected the P contents of these sedimentary rocks. Foremost, variability in the mineralogy of ironstones is an important caveat of this study. Ironstones differ in the relative abundance of Fe (oxyhydr)oxides such as hematite and goethite, Fe phyllosilicates such as berthierine and chamosite, and Fe carbonates such as siderite[26,63,66-68]. These minerals vary in the number of Fe atoms per unit mole, as well as their P scavenging capacity[40,69-71]. Previous studies of ironstones have proposed that these mineralogical assemblages represent the final product of a complex series of diagenetic reactions between primary phases (principally chemical weathering products and organic matter), including Fe cycling and reverse weathering leading to phyllosilicate authigenesis[26,66,72,73]. Clearly, this would have affected the P contents of the sediment, and diagenetic effects need to be carefully considered.

In modern marine environments, P is buried as authigenic phosphates (principally apatite), detrital phases, and organic P, and transformations during diagenesis are largely driven by organic matter degradation and the formation of diagenetic apatite which robustly preserves the bulk-rock P content[74]. Observations from modern hydrothermal environments show that the diagenetic transformation of primary ferrihydrite to more stable Fe (oxyhydr)oxide phases can result in significant release of scavenged P[71]. However, in these modern environments, the majority of this P remobilised during early diagenesis is retained within the sediment pile due to the precipitation of authigenic phosphates, or by coprecipitation or re-adsorption onto Fe (oxyhydr)oxides, and changes in sedimentary P/Fe* values are considered to qualitatively reflect changes in ambient P availability[71]. Similarly, there is petrographic evidence reported from ironstones for the precipitation of authigenic phosphates[22,24,26,75,76]. Much of this phosphate authigenesis likely results from the release of P from clays and their exclusion during iron silicate authigenesis, increasing porewater saturation with respect to phosphate minerals such as apatite[26]. Phosphate-rich Phanerozoic ironstones show significant evidence for primary–early diagenetic phosphate authigenesis and phosphatisation of pre-existing minerals (such as P-coated grains and phosphatised skeletal elements) [22,73,77]. Because phosphate minerals such as apatite are relatively immobile during burial[74], it is unlikely that this phosphatisation was driven by P sourced from the underlying strata. The phosphatisation documented in some Phanerozoic ironstones is interpreted to have been driven by the upwelling of P-rich water[22,23,78], and therefore strongly controlled by local P availability, consistent with our interpretations.

Other secular trends in ironstone mineralogy are worthy of consideration. Goethite is more common in Phanerozoic ironstones than those from the Precambrian[26,62,79]. However, hematite-dominated ironstones are also important in the Phanerozoic (including those which were included in this study[66]), and there is significant variability between hematitic ironstones of the Precambrian, indicating that changes in mineralogy are not the primary control on P/Fe* variability. Importantly, because all the ironstones and iron formations in this study have undergone diagenesis, it is unclear how variability in this process could explain the secular trends observed in the compilation. The significant difference in P/Fe* values between Stage II and Stage III ironstones (Table 1, S1) is particularly informative as both intervals are Proterozoic, meaning that these ironstones would have experienced similar environmental conditions, seawater chemistry, and genetic controls. Therefore, we believe that the simplest explanation is that P supply is the primary control on these distributions. Given our approach of using a large dataset covers a wide range of depositional environments, we believe that it is unlikely that diagenetic loss from ironstones is responsible for the lower P contents of Precambrian ironstones, given that this should correspond to a significant P sink elsewhere which is not recorded by our dataset. However, we acknowledge that this leaves scope for a more detailed study of how the P contents of ironstones is affected by mineralogy and diagenetic transformations.

A clear feature of the ironstone and iron formation records is the variability expressed within units, which may be partly explained by the early diagenetic processes outlined

above. Iron formations can exhibit significant variability in P contents when analysed at the sub-centimetre scale. Some continental margin iron formations contain thin (<1 cm) phosphate-rich laminae[80], yet overall bulk-rock P/Fe* values are low. Similarly, ironstones are characterised by a patchy distribution of authigenic phosphates[24,26,75,76] (as well as phosphate biomineralisation where shells are present). Therefore, much of the variability can likely be explained as a nugget effect, and clearly P/Fe* values from a single sample cannot be simply converted into a seawater P concentration. However, considering P enrichment over an entire sample suite (and statistical representations of this spread such as the median and interquartile range of P/Fe* values; Fig. 2) gives a qualitative representation of the extent of local P burial, which ultimately depends upon synsedimentary P availability.

Ironstones and iron formations tend to retain their original marine P concentrations over geological time, despite often extensive post-depositional alteration. Experimental evidence shows a limited effect on P remobilisation from iron formations during metamorphism[81]. The vast majority of ironstones, including those from the Proterozoic, have experienced negligible to low-grade metamorphism[26,63]. Paragenetic studies of hydrothermally altered and metamorphosed ironstones further indicate that while P can be transformed from sedimentary phases (e.g., francolite), it is retained within the rock as authigenic phosphates[82]. Multiple geochemical studies have demonstrated that modern weathering processes do not appear to significantly alter the bulk-rock P/Fe* values in iron formations (Fig. S2a), with only the thin (~1 mm), weathered surficial crust being affected[83]. Even ore-forming processes, in many cases, do not result in a significantly

different bulk-rock P/Fe* value (Fig. S2a), with secondary phosphates only becoming an issue when an iron formation has undergone extreme supergene metasomatic leaching and replacement by goethite[84] (i.e., sample types not included in this study). The influence of weathering on ironstone geochemistry has not been as extensively explored, and these deposits are more reactive during weathering due to the lack of porosity-occluding chert cement. Nevertheless, comparisons of outcrop and drill core samples from the same region show no significant difference in P/Fe* values for ironstones (Fig. S2b). Given that weathering processes are more likely to increase (rather than decrease) P/Fe* values due to removal of more mobile minerals (compared to phosphates), it is difficult to explain the persistently low values in ironstones throughout the Proterozoic through weathering alone. Thus, the trends in ironstone and iron formation P/Fe* values likely reflect primary depositional processes rather than post-depositional alteration.

Data availability

All data from this study are included in the Supplementary Information.

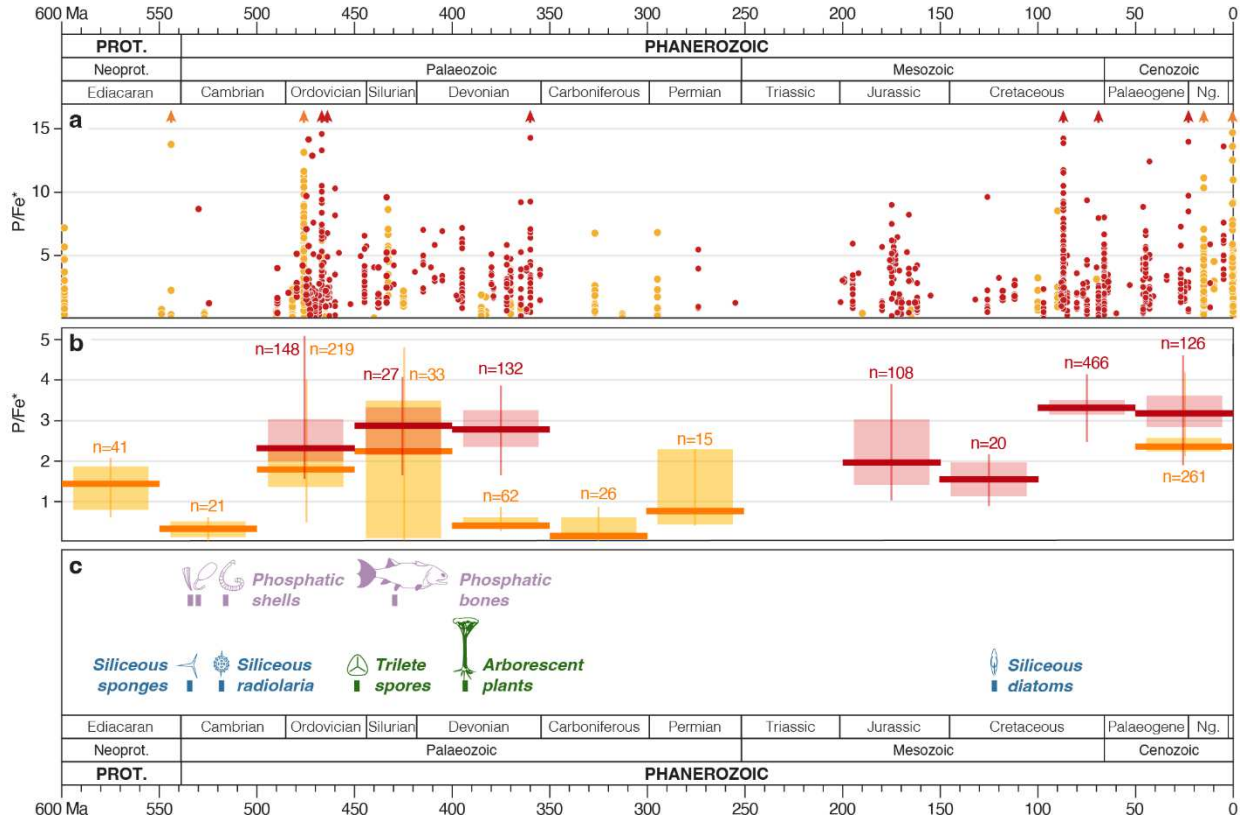
Acknowledgements

This work was supported by grants awarded to C.L.W. and B.W. from National Natural Science Foundation of China (42325206, 42150104), the National Key R&D Program of China (2024YFF0810200), and the Strategy Priority Research Program (Category B) of Chinese Academy of Sciences (XDB0710000). GH was supported by an NSERC Discovery grant (RGPIN-2023-03514) and the Fonds de recherche du Québec (FRQ) [https://doi.org/10.69777/377326]. A.H. acknowledges funding from an ARC DECRA

DE190100988. We acknowledge Dr. Dan Asael for help with geochemical analyses, and Dr. Sam Boone for helpful discussions. This project benefited from the material support and scientific insights of Prof. Noah Planavsky at Yale University.

Author contributions

M.L., C.L.W., L.J.R., and B.W. designed the project. M.A.L., C.L.W., S.P., D.C., N.G., I.H. provided samples. M.L., C.L.W. and L.J.R. conducted geochemical analyses. M.L. and C.L.W. compiled data from the literature. M.L. wrote the manuscript with input from all co-authors.



Extended Data Fig. 1. Detailed view of the temporal variation in the ironstone and exhalative iron formation data of Stage V. **a.** Compilation of P/Fe* values for shallow marine ironstones and exhalative Iron formations. Arrows represent extreme P enrichments (P/Fe* > 15). **b.** Median values (horizontal bars) with 95 % confidence intervals (CI; boxes) and interquartile range (vertical lines) for the P/Fe* data in panel a (note the change in scale), binned into 50-million-year time intervals. Intervals with insufficient samples (n < 15) are not shown. **c.** Fossil distribution showing the first appearance of phosphatic shells and bones[53] (pink), siliceous biomineralisers[54] (blue), and key groups in land plant evolution[61] (green).

Methods References

62 Wang, C. *et al.* Strong evidence for a weakly oxygenated ocean–atmosphere system during the Proterozoic. *Proceedings of the National Academy of Sciences* (2022).

63 Petránek, J. & Van Houten, F. B. *Phanerozoic Ooidal Ironstones: Contribution to the International Geological Correlation Programme, Project 277-Phanerozoic Ooidal Ironstones*. Vol. 7 (Czech geological survey, 1997).

64 Gross, G. A. *Geology of iron deposits in Canada*. (Department of Mines and Technical Surveys, Canada, 1965).

65 Lechte, M. A. *et al.* Subglacial meltwater supported aerobic marine habitats during Snowball Earth. *Proceedings of the National Academy of Sciences* **116**, 25478-25483 (2019).

66 Matheson, E. & Pufahl, P. K. Clinton ironstone revisited and implications for Silurian Earth system evolution. *Earth Science Reviews* (2021).

67 Rudmin, M., Mazurov, A. & Banerjee, S. Origin of ooidal ironstones in relation to warming events: Cretaceous-Eocene Bakchar deposit, south-east Western Siberia. *Marine and Petroleum Geology* **100**, 309-325 (2019).

68 James, H. L. *Chemistry of the iron-rich sedimentary rocks*. (US Government Printing Office, 1966).

69 Berner, R. A. Phosphate removal from sea water by adsorption on volcanogenic ferric oxides. *Earth and Planetary Science Letters* **18**, 77-86 (1973).

70 Feely, R. A. *et al.* The effect of hydrothermal processes on midwater phosphorus distributions in the northeast Pacific. *Earth and Planetary Science Letters* **96**, 305-318 (1990).

71 Poulton, S. W. & Canfield, D. E. Co-diagenesis of iron and phosphorus in hydrothermal sediments from the southern East Pacific Rise: Implications for the evaluation of paleoseawater phosphate concentrations. *Geochimica et Cosmochimica Acta* **70**, 5883-5898 (2006).

72 Young, T. P. Phanerozoic ironstones: an introduction and review. *Geological Society, London, Special Publications* **46**, ix-xxv (1989).

73 Pufahl, P. K. & Grimm, K. A. Coated phosphate grains: Proxy for physical, chemical, and ecological changes in seawater. *Geology* **31**, 801-804 (2003).

74 Ruttenberg, K. C. & Berner, R. A. Authigenic apatite formation and burial in sediments from non-upwelling, continental margin environments. *Geochimica et cosmochimica acta* **57**, 991-1007 (1993).

75 Qiu, Y., Zhao, T. & Li, Y. The Yunmengshan iron formation at the end of the Paleoproterozoic era. *Applied Clay Science* **199**, 105888 (2020).

76 Rudmin, M. *et al.* Minerals of rare earth elements in high-phosphorus ooidal ironstones of the western Siberia and Turgai depression. *Minerals* **10**, 11 (2020).

77 Franceschelli, M., Puxeddu, M. & Carta, M. Mineralogy and geochemistry of Late Ordovician phosphate-bearing oolitic ironstones from NW Sardinia, Italy. *Mineralogy and Petrology* **69**, 267-293 (2000).

78 Dunn, S. K., Pufahl, P. K., Murphy, J. B. & Lokier, S. W. Middle Ordovician upwelling-related ironstone of North Wales: coated grains, ocean chemistry, and biological evolution. *Frontiers in Earth Science* **9**, 669476 (2021).

79 Galili, N. *et al.* The geologic history of marine dissolved organic carbon from iron oxides. *Nature*, 1-7 (2025).

80 Lantink, M. L. *et al.* Precessional pacing of early Proterozoic redox cycles. *Earth and Planetary Science Letters* **610**, 118117 (2023).

81 Schad, M. *et al.* Phosphate remobilization from banded iron formations during metamorphic mineral transformations. *Chemical Geology* **584**, 120489 (2021).
82 Moëlo, Y., Rouer, O. & Bouhnik-Le Coz, M. From diagenesis to hydrothermal recrystallization: polygenic Sr-rich fluorapatite from the oolitic ironstone of Saint-Aubin-des-Chateaux (Armorican Massif, France). *European Journal of Mineralogy* **20**, 205-216 (2008).
83 Li, Z. *et al.* How does weathering influence geochemical proxies in Paleoproterozoic banded iron formations? A case study from outcrop samples of 2.46 Ga banded iron formation, Hamersley Basin, Western Australia. *Geological Society of America Bulletin* (2023).
84 Dukino, R., England, B. & Kneeshaw, M. Phosphorus distribution in BIF-derived iron ores of Hamersley Province, Western Australia. *Applied Earth Science* **109**, 168-176 (2000).

Table 1. Summary of the sedimentary P archives in Stages I–V, as recorded by ironstone, iron formations, phosphorites and shales.

Stage	**Ironstones**	**Iron formations**	**Phosphorites**	**Shales**
Stage I: the Archaean Eon (>2.5 Ga)	Absent	P/Fe* values are consistently low **Exhalative:** *Median 0.30, 3Q 0.51, 95% CI 0.28–0.32* *n = 1006, 64 deposits* **Continental margin:** *Median 0.27, 3Q 0.42, 95% CI 0.23–0.30* *n = 301, 19 deposits* **Granular:** *Median 0.13, 3Q 0.16* *n = 7; 1 deposit*	Absent	Low P contents
Stage II: the Palaeoproterozoic Era (ca. 2.5–1.6 Ga)	Increasing P/Fe* values, but variable *Median 0.74, 3Q 1.62, 95% CI 0.55–0.97* *n = 138, 7 deposits*	P/Fe* values are consistently low **Exhalative:** *Median 0.38, 3Q 0. 68, 95% CI 0.30–0.56* *n = 72, 10 deposits* **Continental margin:** *Median 0.24, 3Q 0.46, 95% CI 0.22–0.26* *n = 661, 36 deposits* **Granular:**	Phosphorites largely deposited in coastal settings Deposition of the oldest phosphorites ca. 2.2 Ga Global phosphorite deposition at ca. 2.0 Ga First appearance of thick (>5 m) phosphorites ca. 1.85–1.7 Ga	Low P contents

		Median 0.16, 3Q 0.35, 95% CI 0.15–0.18 *n = 510; 14 deposits*		
Stage III: the Mesoproterozoic to early Neoproterozoic (ca. 1.6–0.85 Ga)	Rare, P/Fe* values are consistently low *Median 0.11, 3Q 0.23, 95% CI 0.10–0.13* *n = 273; 5 deposits*	Rare, P/Fe* values are consistently low **Exhalative:** *Median 0.14, 3Q 0.18, 95% CI 0.11–0.16* *n = 60; 5 deposits* **Continental margin:** Absent **Granular:** Absent	Rare to absent	Low P contents
Stage IV: the late Tonian to Ediacaran periods (ca. 0.85–0.54 Ga)	Rare, but higher P/Fe* values than Stage III *Median 1.57, 3Q 1.87, 95% CI 0.99–1.85* *n = 14; 1 deposit*	Statistically higher P/Fe* values than previous stages **Exhalative:** *Median 1.17, 3Q 2. 14, 95% CI 1.00–1.33* *n = 258; 14 deposits* **Continental margin:** Absent **Granular:** Absent **Glacial:** *Median 0.86, 3Q 1.76; 95% CI 0.79–0.93* *n = 653; 20 deposits*	Laminated and nodular phosphate in offshore marine shales; reworked granular phosphate Phosphogenesis in offshore environments influenced by upwelling	P-rich shales first start to appear

Stage V: the Phanerozoic Eon (<0.54 Ga)	High P/Fe* values, with secular variation Widespread and P-rich in the early Phanerozoic (Cambrian–early Carboniferous; ca. 0.54–0.35 Ga). Near-absent and low-P in the middle Phanerozoic (middle Carboniferous–Triassic; 0.35–0.2 Ga). Abundant and highly enriched in the late Phanerozoic (Jurassic–modern; ca. 0.2–0 Ga) *Median 3.06, 3Q 4.18, 95% CI 2.94–3.19* *n = 1083; 124 deposits*	High P/Fe* values, with secular variation **Exhalative:** *Median 2.14, 3Q 3.76, 95% CI 1.85–2.24* *n = 650; 35 deposits* Abundant with high P/Fe* values during the early and late Phanerozoic; rarer middle Phanerozoic exhalative iron formations have low P/Fe* values	Phosphorites deposited throughout the Phanerozoic Metre-scale phosphorites are more common in the early and late Phanerozoic	P-rich shales are widespread

Supplementary Files

This is a list of supplementary files associated with this preprint. Click to download.

- SupplementaryInformation.docx
- SupplementarydatatableRevisedFinal.xlsx